Eur. Phys. J. C (2021) 81:394
https://doi.org/10.1140/epjc/s10052-021-09155-z

THE EUROPEAN PHYSICAL JOURNAL C

Regular Article - Theoretical Physics

Constraint on primordial magnetic fields in the light of ARCADE 2 and EDGES observations

Pravin Kumar Natwariya[1,2,a]

[1] Physical Research Laboratory, Theoretical Physics Division, Ahmedabad 380 009, India
[2] Department of Physics, Indian Institute of Technology, Gandhinagar 382 424, India

Received: 10 December 2020 / Accepted: 18 April 2021

Abstract We study the constraints on primordial magnetic fields (PMFs) in the light of the Experiment to Detect the Global Epoch of Reionization Signature (EDGES) low-band observation and Absolute Radiometer for Cosmology, Astrophysics and Diffuse Emission (ARCADE 2). ARCADE 2 observation detected extra-galactic excess radio radiation in the frequency range 3–90 GHz. The enhancement in the radio radiation is also supported by the first station of the Long Wavelength Array (LWA1) in the frequency range 40–80 MHz. The presence of early radiation excess over the cosmic microwave background can not be completely ruled out, and it may explain the EDGES anomaly. In the presence of decaying PMFs, 21 cm differential brightness temperature can modify due to the heating of the gas by decaying magnetic fields, and we can constraint the magnetic fields. For excess radiation fraction (A_r) to be LWA1 limit, we show that the upper bound on the present-day magnetic field strength, B_0, on the scale of 1 Mpc is $\lesssim 3.7$ nG for spectral index $n_B = -2.99$. While for $n_B = -1$, we get $B_0 \lesssim 1.1 \times 10^{-3}$ nG. We also discuss the effects of first stars on IGM gas evolution and the allowed value of B_0. For A_r to be LWA1 limit, we get the upper constraint on magnetic field to be $B_0(n_B = -2.99) \lesssim 4.9 \times 10^{-1}$ nG and $B_0(n_B = -1) \lesssim 3.7 \times 10^{-5}$ nG. By decreasing excess radiation fraction below the LWA1 limit, we get a more stringent bound on B_0.

1 Introduction

The 21 cm signal, due to the hyperfine transition between 1S singlet and triplet states of the neutral hydrogen atom, is a treasure trove to provide an insight into the period when the galaxies and first stars formed. Recently, the EDGES collaboration observed an absorption signal in the redshift range $15 \lesssim z \lesssim 20$. It is nearly two times more than the theoretical prediction based on the ΛCDM framework cosmological scenarios [1,2]. During the cosmic dawn, in the standard cosmological scenario, the temperature of the gas ($T_{\rm gas}$) and cosmic microwave background radiation (CMBR), $T_{\rm CMB}$, varies adiabatically. $T_{\rm gas}$ and $T_{\rm CMB}$ varies with the redshift as $\propto (1+z)^2$ and $\propto (1+z)$ respectively, and temperatures of both the gas and CMBR found to be ~ 6.7 K and ~ 49.1 K at the redshift $z = 17$ respectively (for example see the Refs. [3–5]). EDGES observation reported that the best fitting 21 cm model yields an absorption profile centred at 78 ± 1 MHz and in symmetric "U" shaped form having an amplitude of $T_{21} = -0.5^{+0.2}_{-0.5}$ K with 99% confidence intervals [1]. It is argued that to explain the EDGES observation, for the best fitting amplitude at the centre of the "U" profile, either the cosmic background radiation temperature $T_R \gtrsim 104$ K for the standard $T_{\rm gas}$ evolution or $T_{\rm gas} \lesssim 3.2$ K in the absence of any non-standard evolution of the T_R, i.e. $T_R = T_{\rm CMB}$ [1]. In the standard scenarios, background radiation is assumed to be solely contribution by the cosmic microwave background (CMB).

Although the contribution to the background radiation is assumed to be CMB radiation, the EDGES anomaly encouraged to develop the alternative models in which radio background enhanced [1,6,7]. Recently, the Absolute Radiometer for Cosmology, Astrophysics and Diffuse Emission (ARCADE 2) collaboration, a double-nulled balloon-borne instrument with seven radiometers, detected the excess radio radiation in frequency range 3–10 GHz. It agrees with CMBR at the large frequency (> 1 GHz) but significantly deviates at small frequency [6,8]. This radio radiation is several times larger than the observed radio count due to the known processes [9]. Although in the Ref. [10], authors discuss that merger of the clusters can generate the radio excess in the presence of magnetic turbulence, the presence of early excess radiation can not be completely ruled out. For example, in the redshift range $z \approx 30$ to 16, accretion onto the first

[a] e-mail: pravin@prl.res.in (corresponding author)

Published online: 06 May 2021

intermediate-mass Black Holes can produce a radio radiation [11]. Subsequently, accreting supermassive black holes [12] or supernovae [13] can also produce radio background due to synchrotron emission at the time of cosmic down by accelerated electrons in the presence of the magnetic field. The enhancement in the background radiation is also supported by the first station of the long wavelength array (LWA1) in frequency range 40–80 MHz, and it is modelled by a power law with a spectral index (β) of -2.58 ± 0.05 [14], while ARCADE 2 is modelled with $\beta = -2.62 \pm 0.04$ [6,8].

Origin and evolution of primordial magnetic fields (PMFs) are one of the outstanding problems of cosmology (Ref. [15] and references therein). Presence of decaying PMFs can heat the gas above the 6.7 K at $z = 17$, and even it can erase the EDGES absorption signal [5,16,17]. Still, the EDGES absorption signal can be explained by considering the possible early excess of radio radiation [6]. In the present work, we consider decaying magnetohydrodynamics (MHD) and constraint the present-day strength of primordial magnetic fields. Observations suggest that the magnetic fields (MFs) are present on the length scale of galaxies to the clusters. Recently in the Ref. [18], authors show that PMFs can be used as a remedy to resolve the Hubble tension between different observations. The present-day amplitude of these MFs is constrained from the big bang nucleosynthesis, formation of structures and cosmic microwave background anisotropies and polarization [17,19,20]. Authors of the Ref. [16], put a upper constraint on PMFs strength $B_{1\mathrm{Mpc}} \lesssim 10^{-10}$ G at the length-scale of 1 Mpc by considering $T_{\mathrm{gas}} \lesssim T_{\mathrm{CMB}}$ (i.e. $T_{21} \lesssim 0$) so that, PMFs can not erase the absorption signal in the redshift range $15 \lesssim z \lesssim 20$. Planck 2015 results put upper constraints on PMFs of the order of the $\sim 10^{-9}$ G for different cosmological scenarios [21]. The authors of the Ref. [22], in the context of EDGES observation, put an upper and lower constraint on the PMFs to be 6×10^{-3} nG and 5×10^{-4} nG respectively. Also, the lower bound on the present-day strength of PMFs found in Refs. [23–25]. Subsequently, in the Ref. [26], authors put a lower bound on the strength of intergalactic magnetic fields of the order of 3×10^{-16} G using Fermi observations of TeV blazars. Upper constraint on the PMFs at the end of big bang nucleosynthesis found to be 2×10^{9} G [27]. Presence of strong PMFs can modify the present-day relic abundance of He^4 and other light elements. Therefore, Using the current observation of light element abundances, present-day MFs can be constrained [17,28–31]. The authors of the Ref. [32], put a constraint on the upper bound of PMFs strength of 47 pG for scale-invariant PMFs by comparing CMB anisotropies, reported by the WMAP and Planck, with calculated CMB anisotropies. Generation of the magnetic fields in the early Universe for the various cosmological scenarios has been studied in the earlier literature (for example see Refs. [23,33–36]). It is to be noted that decaying MHD has been studied in several literatures. In these works, the authors consider the decay of the PMFs by ambipolar diffusion and turbulent decay [5,16,17,37,38]. Ambipolar diffusion of magnetic fields is important in neutral medium as it is inversely proportional to free-electron fraction (X_e) and $X_e \sim 10^{-4}$ after redshift $z \lesssim 100$ [5,17,39]. Magnetic energy dissipation into gas, due to ambipolar diffusion, happens because of relative velocity between ion and neutral components of gas [40]. After the recombination ($z \sim 1100$), the radiative viscosity of fluid dramatically decreases, and velocity perturbations are no longer damped, and tangled magnetic fields having length scale smaller than the magnetic Jeans length can dissipate via another mode–turbulent decay [5,17,41]. Magnetic heating of the gas due to the turbulent decay decreases with redshift but later when ionization fraction decreases, heating increases due to ambipolar diffusion [5,17].

In the present work, we use the EDGES signal in the presence of excess radio radiation to constrain the strength of PMFs. Some of the processes which we have discussed responsible for the excess radio radiation can occur at earlier redshift ($z \sim 17$) [11–13]. One the interesting proposal in the Ref. [6], is to argue that such a possibility can exist at the earlier time also, and it can help to explain the EDGES signal. Authors show that the absorption signal can be explained by having excess radio radiation which is around 10% of the observed (excess) radiation of ARCADE 2. In Refs. [42,43], the authors claim that thermal emission from the axion quark nugget dark matter model can explain the EDGES signal, and it can also contribute a fraction of the radiation excess observed by ARCADE 2. At present, there exist several theoretical models to explain this excess at the time of cosmic down. Recently it was argued that, stimulated emission from Bose (axion) stars can give a large contribution to the radio background possibly explaining EDGES and ARCADE 2 observations [44]. In the Ref. [45], the authors consider accreting Pop III black holes and shows that radio emission from these sources can produce the EDGES like signal by increasing background radiation temperature. In other scenarios, the EDGES anomaly can be explained by axion-photon conversion in the presence of intergalactic magnetic fields [46] or by radiative decays of standard model neutrino induced by magnetic fields [47]. Radio excess can also be explained by the cusp region of superconducting cosmic strings [48]. In Ref. [49], authors consider radiative decays of relic neutrino and show that it can potentially explain the ARCADE 2 excess together with the EDGES signal. Depending on the origin, the excess fraction of radio radiation can have a different value. We discuss the constraints on excess radiation later. Considering the above possibilities of having early excess radiation, we believe that it is important to analyze constraints on the primordial magnetic field in the presence of such radiation.

This work is organized in the following sections: in Sect. 2, we discuss the 21 cm signal due to the hyperfine transition between triplet and singlet state of the neutral hydrogen atom. We also discuss 21 cm differential brightness temperature due to the deviation of spin temperature from the background radiation temperature. In Sect. 3, the evolution of the gas temperature and ionization fraction in the presence of decaying PMFs is discussed. Next, in Sect. 4, we consider the effects on the IGM temperature due to first stars. In Sect. 5, we discuss our results and obtain upper constraint on the present day strength of PMFs in the absence/presence of X-ray and VDKZ18 heating [50].

2 21 cm differential brightness temperature

After the recombination, the baryon number density mostly dominated by the neutral hydrogen ($N_{\rm HI}$) and some fraction of residual free electrons ($X_e = N_e/N_H$) and protons ($X_p = N_p/N_H$). Here, N_e, N_p and N_H are number density of free electrons, protons and hydrogen nuclei respectively. The hyperfine interaction in neutral hydrogen atom splits it's ground state into 1S triplet (n_1) and singlet (n_0) hyperfine levels. The Relative number density of hydrogen atom in triplet (n_1) and singlet (n_0) state is characterized by spin temperature (T_S),

$$\frac{n_1}{n_0} = \frac{g_1}{g_0} \times \exp\left(-2\pi\,\nu_{10}/T_S\right), \tag{1}$$

here, g_1 and g_0 are statistical degeneracy of triplet and singlet states respectively and $\nu_{10} = 1420\,\text{MHz} = 1/(21\,\text{cm})$ is corresponding frequency for hyperfine transition. In the context of cosmological scenarios, the spin temperature may depend on collisions between hydrogen atoms, absorption/ emission of background radiation and Ly-α radiation emitted from the first stars. Therefore, the spin temperature can be defined by requiring equilibrium balance between the populations of triplet and singlet state [2,51,52],

$$T_S^{-1} = \frac{T_R^{-1} + x_\alpha T_\alpha^{-1} + x_c T_{\rm gas}^{-1}}{1 + x_\alpha + x_c}\,. \tag{2}$$

Here, $T_{\rm gas}$ is the kinetic temperature of the gas, and T_R is the background radiation temperature. As discussed in the introduction, the possibility of an excess radio radiation background over the CMBR can not be denied. For the excess radio background, we consider the phenomenological model following the Ref. [53]. Here, Authors consider a uniform redshift-independent synchrotron-like radiation, motivated by the ARCADE2 and LWA1 observations. This model can explain the EDGES anomaly in addition to enhancement of cosmic down power spectrum. Accordingly, following the Refs. [7,53–56],

$$T_R = T_0\,(1+z)\left[1 + A_r\left(\frac{\nu_{\rm obs}}{78\,\text{MHz}}\right)^{\beta}\right], \tag{3}$$

where, $T_0 = 2.725$ K is the present day CMB temperature and $\beta = -2.6$ is the spectral index. A_r is the amplitude defined relative to the CMB at reference frequency of 78 MHz. For the 21 cm signal $\nu_{\rm obs}$ is $1420/(1+z)$ MHz. Authors of the Ref. [53], put a limit on the excess radiation background to $1.9 < A_r < 418$ at reference frequency of 78 MHz by considering the effect of an uniform radiation excess on the 21 cm signal from the cosmic dawn, dark ages and reionization. Authors consider a synchrotron-like spectrum with spectral index -2.6. The case with $A_r \sim 418$ corresponds to the LWA1 limit on A_r at the reference frequency of 78 MHz [14,53]. The stringent constraint on excess radiation comes from the Low-Frequency Array (LOFAR) to $A_r < 182$ (95 percent CL) and $A_r < 259$ (99 percent CL) at a reference frequency of 78 MHz and spectral index -2.6 [7]. $T_\alpha \approx T_{\rm gas}$ is the colour temperature due to Lyα radiation from the first stars [51,57]. x_c and x_α are collisional and Wouthuysen-Field (WF) coupling coefficients, respectively [51,57–59],

$$x_c = \frac{T_{10}}{T_R}\frac{C_{10}}{A_{10}}, \quad x_\alpha = \frac{T_{10}}{T_R}\frac{P_{01}}{A_{10}}, \tag{4}$$

here, $T_{10} = 2\pi\,\nu_{10} = 5.9 \times 10^{-6}$ eV and $C_{10} = N_i k_{10}^{iH}$ is collision deexcitation rate. i stands for hydrogen atom, electron and proton. k_{10}^{iH} is the spin deexcitation specific rate coefficient due to collisions of species i with hydrogen atom [2]. $P_{01} = 4P_\alpha/27$ and P_α is scattering rate of Lyα radiation [2]. $A_{10} = 2.86 \times 10^{-15}\ \text{s}^{-1}$ is the Einstein coefficient for spontaneous emission from triplet to singlet state.

The 21 cm differential brightness temperature is given by [1,2,60],

$$T_{21} \approx 23 x_{\rm HI}\left[\frac{0.15}{\Omega_{\rm m}h^2}\,\frac{1+z}{10}\right]^{1/2}\left(\frac{\Omega_{\rm b}h^2}{0.02}\right)\left(1 - \frac{T_R}{T_S}\right)\ \text{mK}, \tag{5}$$

here, $x_{\rm HI} = N_{\rm HI}/N_H$ is the neutral hydrogen fraction. For this work, we consider the following values for the cosmological parameters: $\Omega_{\rm m} = 0.31$, $\Omega_{\rm b} = 0.048$, $h = 0.68$, $\sigma_8 = 0.82$ and $n_s = 0.97$ [61]. As $T_{21} \propto (T_S - T_R)$, there can be three scenarios. If $T_S = T_R$ then $T_{21} = 0$ and there will not be any signal. For the case when $T_S > T_R$, emission spectra can be observed, and when $T_S < T_R$, it leaves an imprint of absorption spectra. 21 cm signal evolution can be described as: after recombination ($z \sim 1100$) to $z \sim 200$, gas and cosmic background radiation shares same temperature and maintain thermal equilibrium due to the Compton scattering. Therefore, $T_{21} = 0$ and the signal is not observed. After $z \sim 200$ until $z \sim 40$, gas decouples from background

radiation and temperature falls as $T_{\rm gas} \propto (1+z)^2$. It implies early absorption spectra of 21 cm signal. Nevertheless, this signal is not observed due to the poor sensitivity of radio antennas. The sensitivity falls dramatically below 50 MHz. After $z \sim 40$ to the formation of the first star, number density and temperature of the gas are very small, hence, $x_c \to 0$. Therefore, there is no signal [2,62]. After the first star formation, gas couples to the spin temperature due to Lyα radiation emitted from the first star by Wouthuysen-Field (WF) effect [57,63]. Therefore, $x_\alpha \gg 1$, x_c and absorption spectra can be seen. After $z \sim 15$, X-ray emitted from active galactic nuclei (AGN) starts to heat the gas and emission spectra can be seen [2].

3 Evolution of the gas temperature in the presence of PMFs

In the presence of decaying magnetohydrodynamics effects, the gas temperature can increase. It can even increase above the background radiation and can erase the 21 cm absorption signal reported by EDGES [5,16,17,41]. Therefore, present-day PMFs strength can be constrained by the EDGES observation in the presence of excess radiation reported by ARCADE 2 and LWA1 [1,6,8,14,53,64]. In the presence of turbulent decay and ambipolar diffusion, thermal evolution of the gas with the redshift can be written as [5,17,40,41,65],

$$\frac{dT_{\rm gas}}{dz} = 2\,\frac{T_{\rm gas}}{1+z} + \frac{\Gamma_c}{(1+z)\,H}(T_{\rm gas} - T_{\rm CMB}) - \frac{2}{3\,N_{\rm tot}(1+z)\,H}(\Gamma_{\rm turb} + \Gamma_{\rm ambi}), \tag{6}$$

Here, $N_{\rm tot} = N_H(1 + f_{He} + X_e)$, $f_{He} = 0.079$ and $T_{\rm CMB} = T_0\,(1+z)$ is the cosmic microwave background (CMB) temperature. $H \equiv H(z)$ is the Hubble parameter. At early times, $T_{\rm gas}$ remains in equilibrium with CMB temperature due to Compton scattering. However, the gas temperature will not be strongly affected by the comparatively small amount of energy in the non-thermal radio radiation. Therefore, $T_{\rm gas}$ and T_α can be assumed independent of the excess radiation [6]. Γ_C is the Compton scattering rate, defined as,

$$\Gamma_C = \frac{8\sigma_T \rho_\gamma N_e}{3\,m_e\,N_{\rm tot}}, \tag{7}$$

here, $\rho_\gamma = a_r T_{\rm CMB}^4$, $a_r = 7.57 \times 10^{-16}$ J m$^{-3}K^{-4}$ is the radiation density constant, σ_T is the Thomson scattering cross-section and m_e is the mass of electron. Change in the electron fraction with redshift[3,4,37,66],

$$\frac{dX_e}{dz} = \frac{1}{H(1+z)}\,\frac{\frac{3}{4}R_{Ly\alpha} + \frac{1}{4}\Lambda_{2s,1s}}{\beta_B + \frac{3}{4}R_{Ly\alpha} + \frac{1}{4}\Lambda_{2s,1s}} \times (N_H X_e^2 \alpha_B - 4(1-X_e)\,\beta_B e^{-E_{21}/T_{\rm CMB}}), \tag{8}$$

here, α_B is the case-B recombination coefficient and β_B is the photo-ionization rate. $E_{21} = 2\pi/\lambda_{\rm Ly\alpha}$, $\lambda_{\rm Ly\alpha} = 121.5682 \times 10^{-9}$ meter is the hydrogen Lyα rest wavelength [3]. $\Lambda_{2s,1s} = 8.22$ sec^{-1} is the two photon decay rate of hydrogen and $R_{\rm Ly\alpha} = \frac{8\pi H}{3N_H(1-X_e)\lambda_{\rm Ly\alpha}^3}$ is the Lyα photon escape rate [66]. Heating rate per unit volume due to the ambipolar diffusion ($\Gamma_{\rm ambi}$) and turbulence decay ($\Gamma_{\rm turb}$) is given by [5,17],

$$\Gamma_{\rm ambi} = \frac{(1-X_e)}{\gamma\,X_e\,(M_H N_b)^2}\,\frac{|(\nabla \times \boldsymbol{B}) \times \boldsymbol{B}|^2}{16\,\pi^2}, \tag{9}$$

$$\Gamma_{\rm turb} = \frac{1.5\,m\,\left[\ln(1+t_i/t_d)\right]^m}{\left[\ln(1+t_i/t_d) + 1.5\ln\{(1+z_i)/(1+z)\}\right]^{m+1}} H\,E_B, \tag{10}$$

here, $E_B = B^2/(8\pi)$ is the magnetic field energy density,

$$\frac{dE_B}{dz} = 4\,\frac{E_B}{1+z} + \frac{1}{H\,(1+z)}\,(\,\Gamma_{\rm turb} + \Gamma_{\rm ambi}\,), \tag{11}$$

and $m = 2(n_B+3)/(n_B+5)$. $z_i = 1088$ is the redshift when heating starts due the magnetic fields (recombination epoch), $\gamma = 1.9 \times 10^{14}\,(T_{\rm gas}/{\rm K})^{0.375}{\rm cm}^3/{\rm g/s}$ is the coupling coefficient, $M_{\rm H}$ is the mass of Hydrogen atom and N_b is the number density of baryons. $t_d = 1/\big(k_d\,V_A(k_d,z)\big)$ is the decay time for the turbulence. For matter dominated era, $t_i = 2/\big(3\,H(z_i)\big)$ and $V_A(k_d,z) = B(k_d,z)/\big(4\,\pi\,\rho_b(z)\,\big)^{1/2}$ is the Alfvén wave velocity. $B(k_d,z)$ is the magnetic field strength smoothed over the scale of k_d at redshift z. k_d is constrained by the damping wavenumber of Alfvén wave. PMFs having wavenumber larger than k_d, are strongly damped by the radiative-viscosity [17,41,67–70]. Following the Ref. [16], we take the time evolution of the Alfvén wave damping scale. It is given as $k_d(z) = k_{d,\rm i}\,f(z)$ and $f(z_i) = 1$. Here, $k_{d,\rm i}$ is the damping wavenumber at recombination epoch,

$$k_{d,\rm i} = 2\pi\ {\rm Mpc}^{-1}\left[1.32 \times 10^{-3}\left(\frac{B_0}{\rm nG}\right)^2\left(\frac{0.02}{\Omega_{\rm b}h^2}\right) \times \left(\frac{\Omega_{\rm m}h^2}{0.15}\right)^{1/2}\right]^{-\frac{1}{n_B+5}}. \tag{12}$$

Here, to smooth the magnetic field amplitude over the length scale of $k_{d,\rm i}$, we choose the Gaussian window function in Fourier space (k) as [16,21,71],

$$B_{k_{d,\rm i}}^2 = \int_0^\infty \frac{d^3k}{(2\pi)^3}\,{\rm e}^{-k^2\left(\frac{2\pi}{k_{d,\rm i}}\right)^2} P_B(k) = B_0^2\left[\frac{k_{d,\rm i}}{2\pi\ {\rm Mpc}^{-1}}\right]^{n_B+3}. \tag{13}$$

Here, we consider PMFs power spectrum, $P_B(k)$, as power law in Fourier space [16],

$$P_B(k) = \frac{(2\pi)^2}{\Gamma\big[(n_B+3)/2\big]}\, B_0^2 \left(\frac{k}{\mathrm{Mpc}^{-1}}\right)^{n_B} \mathrm{Mpc}^3. \quad (14)$$

The magnetic field strength on the scale of 1 Mpc, $B^2_{1\ \mathrm{Mpc}} = \int (dk/2\pi)^3\ \exp[-(k/\mathrm{Mpc}^{-1})^2]\ P_B(k) = B_0^2$. As discussed earlier, magnetic fields are strongly damped above inverse length-scale (k_d), therefore, $P_B(k) = 0$ for $k \geq k_d$. Lorentz force and the magnetic energy density can be calculated as [16],

$$|(\nabla \times \boldsymbol{B})\times \boldsymbol{B}|^2 = \int_{k_1,k_2} k_1^2\ P_B(k_1)\ P_B(k_2)\ f^{2n_B+8}(z)\ (1+z)^{10}, \quad (15)$$

here $\int_{k_1,k_2}[\cdots] = \int\int d^3k_1/(2\pi)^3 \times d^3k_2/(2\pi)^3\,[\cdots]$, and

$$E_B = \frac{1}{8\pi}\int \frac{d^3k}{(2\pi)^3}\ P_B(k)\ f^{n_B+3}(z)\ (1+z)^4. \quad (16)$$

We can get the redshift evolution of the function $f(z)$, by substituting Eq. (16) in Eq. (11).

4 Heating of the IGM due to background radiation

After the first star formation ($z \sim 30$), their radiation starts to heat the intergalactic medium (IGM) [52,59,72–76]. Authors of the Ref. [50], suggests that the kinetic temperature of the gas can also increase due the background radiation even in the absence of X-ray heating. The Lyα photons, due to first stars, intermediate the energy transfer between the thermal motions of the hydrogen and background radiation. Authors claim that this correction to the kinetic temperature of the gas is the order of ($\sim 10\%$) at $z = 17$, in the absence of X-ray heating (hereafter we use the term VDKZ18 for this heating of the gas). Following the above reference, the Eq. (6) will modify,

$$\frac{dT_{\mathrm{gas}}}{dz} = \left.\frac{dT_{\mathrm{gas}}}{dz}\right|_{[\mathrm{eq.}(6)]} + \left.\frac{dT_{\mathrm{gas}}}{dz}\right|_{\mathrm{X-ray}} - \frac{\Gamma_R}{(1+z)\,(1+f_{He}+X_e)}, \quad (17)$$

where, $dT_{\mathrm{gas}}/dz\big|_{[\mathrm{eq.}(6)]}$ stands for the gas temperature evolution represented in Eq. (6), and

$$\Gamma_R = x_{\mathrm{HI}}\,\frac{A_{10}}{2\,H}\,x_R\left[\frac{T_R}{T_S}-1\right]T_{10}, \quad (18)$$

here, $x_R = 1/\tau_{21} \times [1-\exp(-\tau_{21})]$, and the 21 cm optical depth $\tau_{21} = 8.1\times10^{-2}\,x_{\mathrm{HI}}\,[(1+z)/20]^{1.5}\,(10\,\mathrm{K}/T_S)$. And, $T_{10} = 2\pi\nu_{10} = 0.0682$ K. To include the X-ray heating of the IGM, we consider the *tanh* parameterization [77–79]. In the presence of X-ray radiation, the ionization fraction evolution with redshift will also change. For the present case, we consider the fiducial model, for X-ray heating and ionization fraction evolution, motivated by Ref. [77]. The heating effects of both the VDKZ18 and X-ray are discussed in plots 1a, b, 2, 3b and 4b.

5 Result and discussion

To study the gas temperature evolution with redshift in the presence of primordial magnetic field dissipation, we solve the coupled equations (6), (8) and (11). To get the Lorentz force term in Eq. (9), we solve the Eq. (15). Similarly, to get the magnetic field energy density in Eq. (10), we solve the Eq. (16). To get the evolution of the $f(z)$ with redshift, $df(z)/dz$, we substitute Eq. (16) in Eq. (11) with initial condition $f(z_i) = 1$. To obtain upper constraint on PMFs strength, we solve the Eq. (5) with Eqs. (6), (8) and (11) for $T_{21} \simeq -300$ mK or $-$ 500 mK by varying B_0, n_B and A_r. For infinite Lyα coupling $T_S \simeq T_{\mathrm{gas}}$, therefore, T_S solely depends on the gas temperature. While, for finite Lyα coupling, T_S depends on both the gas and background radiation temperature.

In Fig. 1, we plot the gas temperature evolution with the redshift for different present-day magnetic field strength and background radiation. The solid blue lines represent the case when there is no heating of the IGM gas, i.e. no X-ray, VDKZ18 or magnetic heating. The pink shaded band in the figure shows the EDGES redshift range, $15 \leq z \leq 20$, for the 21 cm absorption signal. In plot 1a, we consider only VDKZ18 and X-ray heating. The orange dashed line describes the heating due to VDKZ18 only while keeping $A_r = 0$. Next, we increase the value of A_r from 0 to 100. This case is described by the dashed-green line in plot 1a, which shows a significant rise in the gas temperature due to the excess radiation fraction. Further, if one increases the A_r to its LWA1 limit, i.e. $A_r = 418$, the gas temperature does not change significantly from $A_r = 100$ case, as shown by the solid magenta curve. It happens because $\Gamma_R \propto (T_R/T_S - 1) \sim T_R/T_S$, Eq. 18. As we increase A_r, T_R/T_S increases slowly. For example, at $z = 17$, T_R/T_S is 6.5 for $A_r = 0$, 51.4 for $A_r = 100$ and 54.9 for $A_r = 418$. Here, we can see that, even increasing A_r to ~ 4 times (100 to 418), T_R/T_S increases by only 6.8 percent. Therefore, increasing further A_r will not affect gas temperature significantly. To analyse the role of X-ray heating, we have first considered the heating due to X-ray only, depicted by the red dashed line. The inclusion of VDKZ18 for $A_r = 0$ further increases the gas temperature slightly, as shown by the black dashed line. In this case of inclusion of X-ray heating, if we increase the value of A_r to 100, there is a significant increase in the gas temperature as shown by the solid green

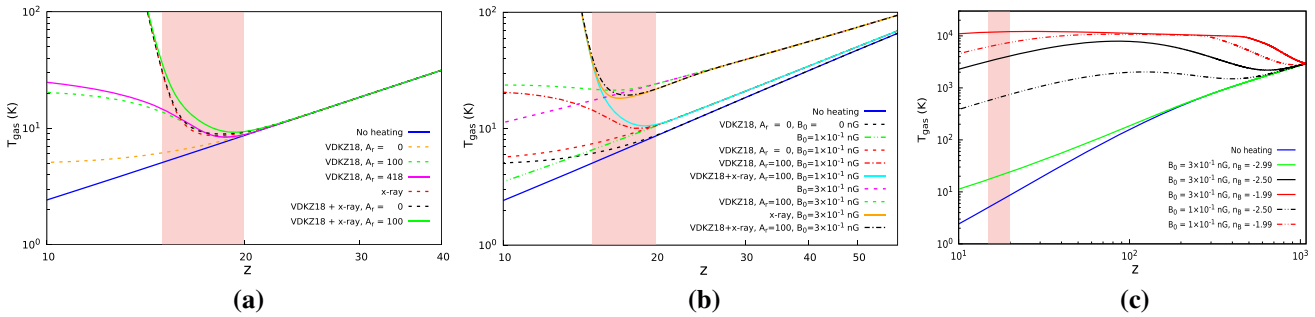

Fig. 1 The gas temperature evolution with redshift. The solid blue lines, in all plots, represent the case when there is no X-ray, VDKZ18 or magnetic heating. VDKZ18 corresponds to the heat transfer from the background radiation to gas mediated by Lyα. The shaded region represents the EDGES observation redshift range, $15 \leq z \leq 20$. In figure **a**, we consider only VDKZ18 and X-ray heating with excess radiation (A_r). In figure **b**, we include different combination of VDKZ18, X-ray and magnetic heating, and spectral index is fixed to -2.99. In figure **c**, we vary the spectral index and plot magnetic heating of the gas

line. We find the contribution due to X-ray heating dominates for redshift values $z \lesssim 15$.

In plot 1a, we compare the contribution of VDKZ18 and X-ray heating. In plot 1b, we compare the contributions of VDKZ18, X-ray and magnetic heating while keeping the spectral-index, $n_B = -2.99$ for a nearly scale-invariant magnetic field spectrum. While in Fig. 1c, we vary the magnetic spectral index (n_B) and plot the magnetic heating of the gas.

In plot 1b, we have included the effect of primordial magnetic fields on the IGM gas evolution. The solid blue line represents the case when there is no heating, and the dashed-black curve shows the case of VDKZ18 with no magnetic fields and X-ray for $A_r = 0$. The double dot-dashed green curve represents the case when there is only the magnetic heating with a magnetic field strength of $B_0 = 1 \times 10^{-1}$nG. Next, we include the case of VDKZ18 for $A_r = 0$ in the pure magnetic heating scenario, as shown by the red dashed curve. Now, if we increase A_r from 0 to 100, the gas temperature rises significantly in the shaded region as shown by the dash-dotted red curve in Fig. 1b. Now the further addition of X-ray heating is shown by the cyan plot, which shows significant heating in the shaded region. Next, for more analysis, we increase the magnetic field strength from $B_0 = 1 \times 10^{-1}$ nG to $B_0 = 3 \times 10^{-1}$ nG and study cases with VDKZ18 and X-ray as before. The magenta dashed line depicts the case with only magnetic heating. The green dashed line shows the case of VDKZ18 with $A_r = 100$. The orange curve shows the case with magnetic and X-ray heating only. Here, as expected, the gas temperature decreases after the inclusion of the X-ray effect with the magnetic fields. It happens because the ionization fraction increases by X-ray radiation. Ambipolar diffusion evolves as $\Gamma_{\rm ambi} \propto (1-X_e)/X_e$; therefore, as ionization fraction increases, ambipolar diffusion of the magnetic field decreases. Thus, the heating due to magnetic fields also decreases. Therefore, including the X-ray contribution with the magnetic field decreases the magnetic field diffusion. Hence, the gas temperature decreases (this effect also occurs for $B_0 = 1 \times 10^{-1}$ nG, but it is not visible in the plot). The black dot-dashed line includes all the three effects: magnetic and X-ray heating together with VDKZ18 for $A_r = 100$ and $B_0 = 3 \times 10^{-1}$ nG. Here, the addition of the VDKZ18 heating for $A_r = 100$ increases the gas temperature above the solid orange line. It is also lower than the magenta dashed line because of the inclusion of the X-ray contribution. At the smaller redshift, X-ray heating dominates over all other heating mechanisms, and all lines merge.

In Fig. 1c, we plot the magnetic heating of the gas for the different spectral index, n_B. The solid lines, except the blue one, represent the magnetic heating for $B_0 = 3 \times 10^{-1}$ nG, while double dot-dashed lines are for $B_0 = 1 \times 10^{-1}$ nG. Increasing the spectral index, the magnetic heating due to ambipolar diffusion and turbulent decay increases as $\Gamma_{\rm ambi} \propto \left(1/\Gamma[(n_B+3)/2]\right)^2$ and $\Gamma_{\rm turb} \propto 1/\Gamma[(n_B+3)/2]$ (by ignoring the logarithmic and integral dependencies). For example, if one changes n_B from its value -2.99 to -1 then $1/\Gamma[(n_B+3)/2]$ changes from 5×10^{-3} to 1. Therefore, by increasing n_B from -2.99 to -1, magnetic heating enhances significantly. To get T_{21} (Eq. (5)) around -500 mK or -300 mK at $z = 17.2$, one needs to ensure that even by increasing n_B, that the factor $x_{\rm HI}(1 - T_R/T_S)$ remains same. Thus from Eqs. (9), (10) and (14) when we increase n_B, we have to decrease B_0 so that the magnetic heating contribution to the gas remains the same. Therefore, by increasing n_B, the upper bound on B_0 will become more stringent. Here, we also include the collisional ionization of the gas in Eq. (8), as this term is important only when gas temperature is $\gtrsim 1.58 \times 10^5$ K. Otherwise this term is exponentially suppressed as $\propto \exp[-(13.6\ {\rm eV})/T_{\rm gas}]$ [17,80,81]. In plot 1c, the gas temperature rises by increasing B_0, as more magnetic energy is getting injected into thermal energy of the gas via $\Gamma_{\rm ambi} \propto E_B^2$ and $\Gamma_{\rm turb} \propto E_B$. However, for redshift $z \lesssim 100$, the gas temperature starts decreasing as the cooling

effect due to expansion of the Universe become dominant, as can be seen in equations (6) and (11) (it also depends on the strength and spectral index of the magnetic field). Since, with the expansion of the Universe, magnetic energy density (E_B) also dilutes, the contributions from $\Gamma_{\rm ambi}$ and $\Gamma_{\rm turb}$ decreases as can be seen from Eqs. (9)–(11).

In Fig. 2a, we plot the spin (dashed lines) and gas (solid lines) temperature. For $A_r = 0$, i.e. $T_R = T_{\rm CMB}$, we get $T_{\rm gas} \simeq T_S$ as seen by the overlapping dashed and solid blue lines in the shaded region. x_α and x_c are $\propto 1/T_R$ as can be seen from Eqs. (2) and (4). Therefore, the coupling between the gas and spin temperature decreases by increasing A_r. As discussed before, increasing the value of A_r above ~ 100, the spin temperature increases, but the increment in gas temperature becomes insignificant, and the T_R/T_S ratio increases slowly. Therefore, as x_α and x_c decreases, the difference between the gas and spin temperature increases, as shown in the plot 2a. Increasing the values of A_r from 100 (green lines) to 418 (black lines), the difference between gas and spin temperatures increases. Figure 2b, shows the plots for 21 cm differential brightness temperature vs. redshift, for all the cases discussed in plot 2a. As we increase the A_r from 0 to 100 the $|T_{21}|$ increases. By increasing A_r from 100 to 418, values of T_{21} does not change significantly. Further, including X-ray heating and magnetic heating (for $B_0 = 3 \times 10^{-1}$ nG and $n_B = -2.99$) the gas temperature rises and $|T_{21}|$ decreases.

In Fig. 3, we plot the maximally allowed values of B_0 versus radiation excess (A_r) for different spectral indexes. The colour-bars represent the variation of the magnetic field spectral index. In the plots, the spectral index varies from its nearly scale-invariant value ($-$ 2.99) to $-$ 1. Here, we consider both the EDGES best fit and upper constraint on the 21 cm absorption signal for constraining B_0. The green-yellow colour scheme represents the case with $T_{21}|_{z=17.2} \simeq -500$ mK, while the red-grey colour scheme represents the case with $T_{21}|_{z=17.2} \simeq -300$ mK. Numerical values of n_B for the different colour bands are written with different colour. For $T_{21}|_{z=17.2} \simeq -300$ mK case the value of n_B written with blue coloured text , while for $T_{21}|_{z=17.2} \simeq -500$ mK case it is written with black coloured text. The colour-bars are common for both the plots.

In Fig. 3a, we consider infinite Lyα coupling ($x_\alpha \gg x_c$, 1), i.e. $T_S \simeq T_{\rm gas}$. Here, we do not consider the X-ray and VDKZ18 effects on the gas and thus the 21 cm signal $T_{21} \propto (1 - T_R/T_{\rm gas})$. As we increase A_r, the amplitude of $|T_{21}|$ increases, and we get more window to increase the gas temperature. In this plot, we consider heating only due to the decaying magnetohydrodynamics. Therefore, we can increase B_0 as we increase A_r. As discussed earlier, by decreasing n_B, the amplitude of the magnetic field power spectrum also decreases, resulting in less magnetic energy dissipation into the gas kinetic energy. Thus by reducing values of n_B from $-$ 1 to $-$ 2.99, we get more window to increase B_0. Next, when one increases T_{21} from $-$ 500 mK to $-$ 300 mK, the allowed value of B_0 also increases. This is shown by the red-grey colour scheme in Fig. 3. In Fig. 3b, we consider the effects of VDKZ18 and X-ray on IGM gas evolution due to first stars after $z \lesssim 35$ and consider finite Lyα coupling. As discussed earlier, $T_{\rm gas} \neq T_S$ for $A_r > 0$ and the difference between gas and spin temperature increases as A_r increases. Thus, in the presence of first star's effects, the upper bound on the present-day strength of PMFs modifies. Following the Refs. [77–79], we consider WF coupling coefficient, $x_\alpha = 2A_\alpha(z) \times (T_0/T_R)$. Here, $A_\alpha(z) = A_\alpha(1 + \tanh[(z_{\alpha 0} - z)/\Delta z_\alpha])$, the step height $A_\alpha = 100$, pivot redshift $z_{\alpha 0} = 17$ and duration $\Delta z_\alpha = 2$. The collisional coupling coefficient, $x_c = T_{10}/T_R \times (N_H\, k_{10}^{HH})/A_{10}$. After the inclusion of X-ray and VDKZ18 heating effects, the gas temperature remains $>$ 10 K. Therefore, we can take $k_{10}^{HH} \approx 3.1 \times 10^{-11}\ (T_{\rm gas}/{\rm K})^{0.357} \exp(-32\ {\rm K}/T_{\rm gas})$ cm^3/sec for 10 K $< T_{\rm gas} <$ 10^3 K. As illustrated in plot 1 and 2, increasing excess radiation fraction A_r above ~ 100,

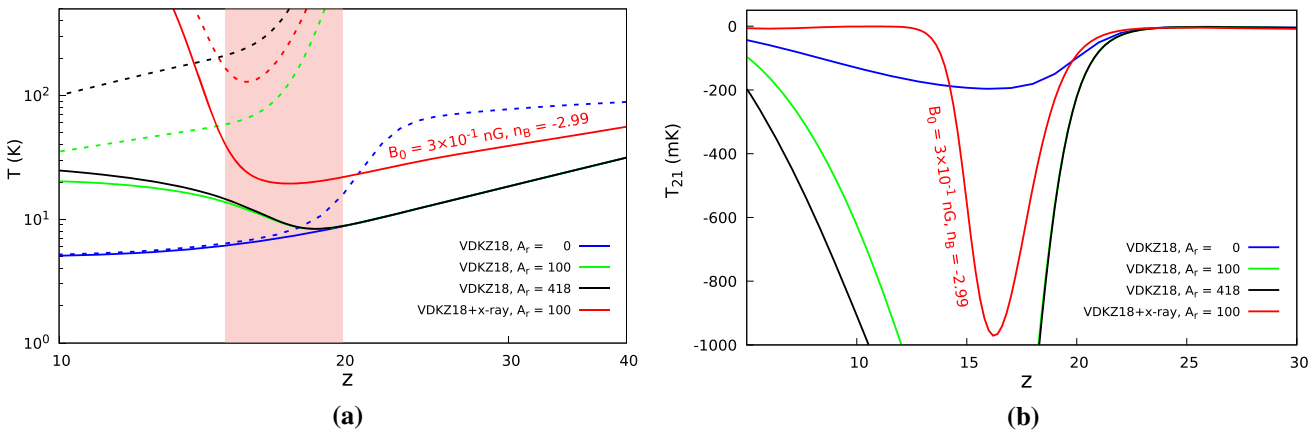

Fig. 2 Plot **a** shows the gas (solid lines) and spin (dashed lines) temperature evolution, The shaded region corresponds to the redshift $15 \leq z \leq 20$ – the redshift range for EDGES reported signal. Plot **b**, shows the 21 cm differential brightness temperature with redshift for same cases in plot **a**

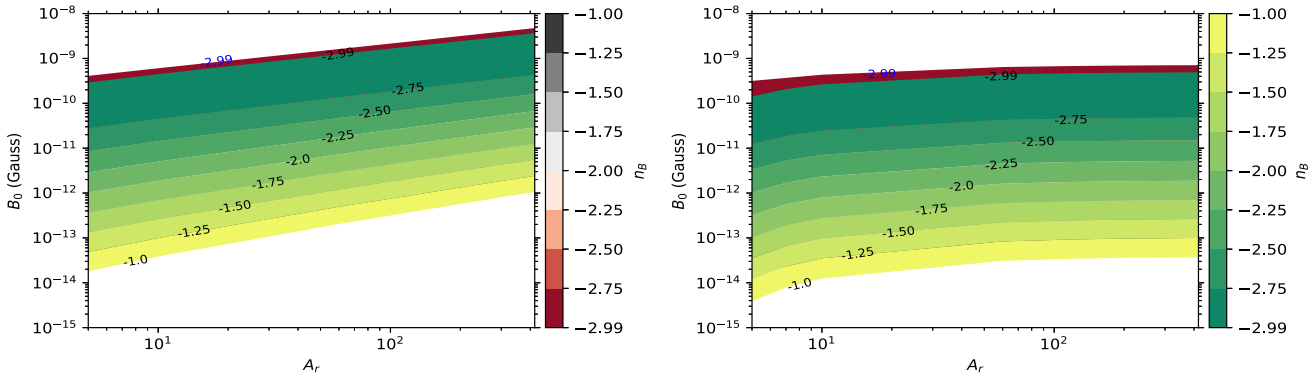

Fig. 3 In these plots, we study upper bounds on present-day magnetic field strength (B_0) with excess radiation fraction (A_r) for different values of the spectral index, n_B. The green-yellow and red-grey colour schemes represent the cases when $T_{21}|_{z=17.2} \simeq -500$ mK and -300 mK, respectively. For $T_{21}|_{z=17.2} \simeq -300$ mK case the value of n_B written with blue coloured text , while for -500 mK case it is written with black coloured text. In plot **a**, we consider $T_S \simeq T_{\rm gas}$ and do not take into account the X-ray and VDKZ18 effects. While in figure **b**, we consider the effects of VDKZ18 and X-ray on IGM gas due to first stars after $z \lesssim 35$ and consider finite Lyα coupling. The colour-bars are common for both plots

the T_R/T_S remains nearly constant and this also mean that T_{21} remain unchanged. Consequently one can not increase the value of B_0 and one gets nearly flat profile for B_0 for $A_r \gtrsim 100$ in Fig. 3b.

In Fig. 4, we plot the maximally allowed values of B_0 vs n_B for various values of A_r. The colour-bars represent the variation in A_r. In the plots, A_r varies from 5 to LWA1 limit ~ 418. We consider both the EDGES best fit and upper constraint on 21 cm absorption signal for constraining B_0. The green-yellow scheme represent the case with $T_{21}|_{z=17.2} \simeq -500$ mK, while the red-grey colour scheme represent the case $T_{21}|_{z=17.2} \simeq -300$ mK. Numerical values of A_r for the different colour bands are written in different colours. For $T_{21}|_{z=17.2} \simeq -300$ mK case the value of A_r written with blue coloured text , while for $T_{21}|_{z=17.2} \simeq -500$ mK case it is written with black coloured text. The spectral index ranges from -2.99 to -1. The red dashed line represents the Planck 2015 upper constraint on the present-day magnetic field strength with spectral index in both plots. This constraint has been taken from Refs. [16,21].

In plot 4a, we consider $T_S \simeq T_{\rm gas}$ and we do not take into account the X-ray and VDKZ18 effects on IGM gas evolution. The zoomed inset in the figure shows the contour plot when $T_{21}|_{z=17.2} \simeq -300$ mK. Here, considering $T_{21}|_{z=17.2} \simeq -300$ mK, for $n_B < -2.98$ the $A_r \gtrsim 200$ is excluded similarly for $n_B < -2.96$ the $A_r \gtrsim 280$ is excluded by Planck 2015 upper constraint on B_0. Likewise, for $T_{21}|_{z=17.2} \simeq -500$ mK, for $n_B < -2.97$ the $A_r \gtrsim 280$ is excluded. For spectral index -2.9 and excess radiation fraction 418, we get the upper constraint on B_0 to be ~ 1 nG and 1.3 nG by requiring $T_{21}|_{z=17.2} \simeq -500$ mK (EDGES best fit constraint) and -300 mK (EDGES upper constraint), respectively. While for $n_B = -1$, these bound change to 1.1×10^{-3} nG and 1.6×10^{-3} nG for $T_{21}|_{z=17.2} \simeq -500$ mK and -300 mK, respectively. In plot (4b), we include both the VDKZ18 and X-ray effect and consider finite Lyα coupling. As discusses earlier, for $A_r \gtrsim 100$, T_R/T_S ratio remain nearly constant. Therefore, in the plot 4b, we can see that for $A_r \gtrsim 100$, the upper bound on B_0 is not changing significantly—the plots are merged for $A_r \gtrsim 100$. These plots have been shown by the zoomed inset. The right upper zoomed inset is shown for $T_{21} \simeq -300$ mK, while left lower zoomed inset is shown for green-yellow contour plots when $T_{21} \simeq -500$ mK. Therefore, further increasing $A_r > 100$ will not change significantly the upper bound on B_0. As illustrated in Figs. 1 and 2, $T_S > T_{\rm gas}$ for $A_r > 0$, and $T_{21} \propto (1 - T_R/T_S)$. Therefore, to get $T_{21} \simeq -300$ mK or -500 mK, we need to lower B_0 compared to previous scenario – Fig. 4a. Hence, we get the more stringent upper bound on present-day magnetic field strength in Fig. 4b. For spectral index -2.9 and excess radiation fraction 418, we get the upper constraint on B_0 to be $\lesssim 1.7 \times 10^{-1}$ nG and 1.2×10^{-1} nG by requiring $T_{21}|_{z=17.2} \simeq -300$ mK and -500 mK, respectively. For $n_B = -1$, we get $B_0 \lesssim 6.9 \times 10^{-5}$ nG and 3.7×10^{-5} nG by requiring EDGES upper and best fit constraint on 21 cm differential brightness temperature. Decreasing the values of A_r, the upper constraint on B_0 becomes more stringent. For example, when $A_r = 5$, we get upper bound on present day magnetic field strength to be $\lesssim 1.4 \times 10^{-1}$ nG for spectral index -2.99, and for spectral index $n_B = -1$ we get $B_0 \lesssim 3.8 \times 10^{-6}$ nG by requiring EDGES best fit constraint on T_{21}. The upper bounds are also well below the Planck 2015 constraint [21].

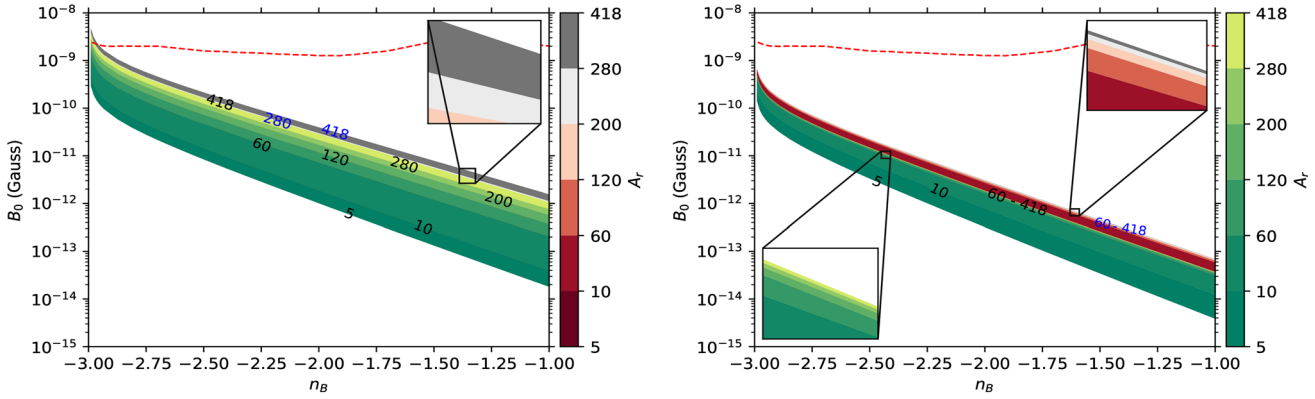

Fig. 4 In these plots, we study upper bounds on the present-day magnetic field strength (B_0) with spectral index (n_B) for different values of excess radiation fraction (A_r). The green-yellow and red-grey colour schemes represent the cases when $T_{21}|_{z=17.2} \simeq -500$ mK and -300 mK, respectively. For $T_{21}|_{z=17.2} \simeq -300$ mK case the value of n_B written with blue coloured text , while for -500 mK case it is written with black coloured text. In plot **a**, we consider $T_S \simeq T_{gas}$ and do not take into account the X-ray and VDKZ18 effects. While in figure **b**, we consider the effects of VDKZ18 and X-ray on IGM gas due to first stars after $z \lesssim 35$ and consider finite Lyα coupling. The colour-bars are common for both plots. The red dashed line depicts the Planck 2015 upper constraint on the present-day magnetic field strength [16,21]

6 Conclusions

In the present work, we study the upper constraint on the strength of the primordial magnetic fields for different spectral index using the bound of EDGES observation on T_{21}, in the presence of uniform redshift-independent synchrotron like radiation reported by ARCADE 2 and LWA1 [6,8,14,53]. We have considered excess radiation fraction up to the LWA1 limit at the reference frequency of 78 MHz, i.e. $A_r \sim 418$ [14,53]. To get the upper constraint on B_0, we have used both the EDGES upper and best-fit constraints on T_{21}. We have considered two scenarios: First, infinite Lyα coupling (i.e. $x_\alpha \gg x_c, 1$) without the effects of X-ray and VDKZ18 on IGM gas evolution. Next, we have considered the finite Lyα coupling with X-ray and VDKZ18 effects. The following summarises our results for $T_{21} = -500$ mK.

In the first scenario, for $A_r = 418$, we get $B_0 \lesssim 3.7$ nG for spectral index -2.99, while for $n_B = -1$ we get $B_0 \lesssim 1.1 \times 10^{-3}$ nG. When $A_r = 5$, upper constraint on present-day magnetic field strength varies from $B_0 \lesssim 2.9 \times 10^{-1}$ nG to 1.8×10^{-5} nG by varying n_B from -2.99 to -1, respectively.

In the second scenario, the upper bounds on B_0 will modify [50,77]. For $A_r = 418$, we get the upper constraint on magnetic field to be $B_0(n_B = -2.99) \lesssim 4.9 \times 10^{-1}$ nG and $B_0(n_B = -1) \lesssim 3.7 \times 10^{-5}$ nG. While for $A_r = 5$, we get upper bound on present day magnetic field strength to be $\lesssim 1.4 \times 10^{-1}$ nG for spectral index -2.99, and for spectral index $n_B = -1$ we get $B_0 \lesssim 3.8 \times 10^{-6}$ nG.

We would like to note that these upper bounds on B_0 that we have reported here are also consistent with the Planck observations [21,82].

Acknowledgements The author would like to thank Prof. Jitesh R. Bhatt for improving the presentation of the manuscript and helpful discussions. The author would also like to thank Prof. Karsten Jedamzik and Alekha C. Nayak for useful comments. All the computations are accomplished on the Vikram-100 HPC cluster at Physical Research Laboratory, Ahmedabad. Finally, the author thanks the Referee for suggestions and a detailed report that significantly improved the quality of the manuscript.

Data Availability Statement This manuscript has no associated data or the data will not be deposited. [Authors' comment: We have not used any experimental data, and references are given for the external data.]

Funded by SCOAP[3].

References

1. J.D. Bowman, A.E.E. Rogers, R.A. Monsalve, T.J. Mozdzen, N. Mahesh, Nature **555**, 67 (2018). https://doi.org/10.1038/nature25792
2. J.R. Pritchard, A. Loeb, Rep. Prog. Phys. **75**, 086901 (2012). https://doi.org/10.1088/0034-4885/75/8/086901
3. S. Seager, D.D. Sasselov, D. Scott, Ast. J. **523**, L1 (1999). https://doi.org/10.1086/312250

4. S. Seager, D.D. Sasselov, D. Scott, ApJ **128**, 407 (2000). https://doi.org/10.1086/313388
5. J. Chluba, D. Paoletti, F. Finelli, J.A. Rubiño-Martín, MNRAS **451**, 2244 (2015). https://doi.org/10.1093/mnras/stv1096
6. C. Feng, G. Holder, Astrophys. J. **858**, L17 (2018). https://doi.org/10.3847/2041-8213/aac0fe
7. R. Mondal, A. Fialkov, C. Fling, I.T. Iliev, R. Barkana, B. Ciardi, G. Mellema, S. Zaroubi, L.V.E. Koopmans, F.G. Mertens, B.K. Gehlot, R. Ghara, A. Ghosh, S.K. Giri, A. Offringa, V.N. Pandey, Mon. Not. R. Astron. Soc. **498**, 4178 (2020). https://doi.org/10.1093/mnras/staa2422. https://www.academic.oup.com/mnras/article-pdf/498/3/4178/33787443/staa2422.pdf
8. D.J. Fixsen, A. Kogut, S. Levin, M. Limon, P. Lubin, P. Mirel, M. Seiffert, J. Singal, E. Wollack, T. Villela, C.A. Wuensche, Astrophys. J. **734**, 5 (2011). https://doi.org/10.1088/0004-637X/734/1/5
9. J. Singal, J. Haider, M. Ajello, D.R. Ballantyne, E. Bunn, J. Condon, J. Dowell, D. Fixsen, N. Fornengo, B. Harms, G. Holder, E. Jones, K. Kellermann, A. Kogut, T. Linden, R. Monsalve, P. Mertsch, E. Murphy, E. Orlando, M. Regis, D. Scott, T. Vernstrom, L. Xu, Publ. Astron. Soc. Pac. **130**, 036001 (2018). https://doi.org/10.1088/1538-3873/aaa6b0
10. K. Fang, T. Linden, J. Cosmol. Astropart. Phys. **2016**, 004 (2016). https://doi.org/10.1088/1475-7516/2016/10/004
11. A. Ewall-Wice, T.-C. Chang, J. Lazio, O. Doré, M. Seiffert, R.A. Monsalve, Astrophys. J. **868**, 63 (2018). https://doi.org/10.3847/1538-4357/aae51d
12. P.L. Biermann, B.B. Nath, L.I. Caramete, B.C. Harms, T. Stanev, J.B. Tjus, Mon. Not. R. Astron. Soc. **441**, 1147 (2014). https://doi.org/10.1093/mnras/stu541
13. R. Jana, B.B. Nath, P.L. Biermann, Mon. Not. R. Astron. Soc. **483**, 5329 (2018). https://doi.org/10.1093/mnras/sty3426
14. J. Dowell, G.B. Taylor, Astrophys. J. **858**, L9 (2018). https://doi.org/10.3847/2041-8213/aabf86
15. K. Subramanian, Rep. Prog. Phys. **79**, 076901 (2016). https://doi.org/10.1088/0034-4885/79/7/076901
16. T. Minoda, H. Tashiro, T. Takahashi, MNRAS **488**, 2001 (2019). https://doi.org/10.1093/mnras/stz1860
17. S.K. Sethi, K. Subramanian, MNRAS **356**, 778 (2005). https://doi.org/10.1111/j.1365-2966.2004.08520.x
18. K. Jedamzik, L. Pogosian, Relieving the hubble tension with primordial magnetic fields. Phys. Rev. Lett. **125**, 181302 (2020). https://doi.org/10.1103/PhysRevLett.125.181302
19. P. Trivedi, T.R. Seshadri, K. Subramanian, PRL **108**, 231301 (2012). https://doi.org/10.1103/PhysRevLett.108.231301
20. P. Trivedi, K. Subramanian, T.R. Seshadri, PRD **89**, 043523 (2014). https://doi.org/10.1103/PhysRevD.89.043523
21. Planck Collaboration et al., A&A **594**, A19 (2016). https://doi.org/10.1051/0004-6361/201525821
22. P.K. Natwariya, J.R. Bhatt, Mon. Not. R. Astron. Soc. Lett. **497**, L35 (2020). https://doi.org/10.1093/mnrasl/slaa108
23. J. Ellis, M. Fairbairn, M. Lewicki, V. Vaskonen, A. Wickens, JCAP **2019**, 019 (2019). https://doi.org/10.1088/1475-7516/2019/09/019
24. The FLAT Collaboration, J. Biteau, ApJS **237**, 32 (2018). https://doi.org/10.3847/1538-4365/aacdf7
25. F. Tavecchio, G. Ghisellini, L. Foschini, G. Bonnoli, G. Ghirlanda, P. Coppi, MNRAS Lett. **406**, L70 (2010). https://doi.org/10.1111/j.1745-3933.2010.00884.x
26. A. Neronov, I. Vovk, Science **328**, 73 (2010). https://doi.org/10.1126/science.1184192
27. B. Cheng, A.V. Olinto, D.N. Schramm, J.W. Truran, PRD **54**, 4714 (1996). https://doi.org/10.1103/PhysRevD.54.4714
28. J.J. Matese, R.F. O'Connell, Phys. Rev. **180**, 1289 (1969). https://doi.org/10.1103/PhysRev.180.1289
29. G. Greenstein, Nature **223**, 938 (1969). https://doi.org/10.1038/223938b0
30. H. Tashiro, N. Sugiyama, MNRAS **368**, 965 (2006). https://doi.org/10.1111/j.1365-2966.2006.10178.x
31. K.L. Pandey, T.R. Choudhury, S.K. Sethi, A. Ferrara, Mon. Not. R. Astron. Soc. **451**, 1692 (2015). https://doi.org/10.1093/mnras/stv1055
32. K. Jedamzik, A. Saveliev, Phys. Rev. Lett. **123**, 021301 (2019). https://doi.org/10.1103/PhysRevLett.123.021301
33. J.M. Quashnock, A. Loeb, D.N. Spergel, ApJ Lett. **344**, L49 (1989). https://doi.org/10.1086/185528
34. D. Grasso, H.R. Rubinstein, Phys. Rep. **348**, 163 (2001). https://doi.org/10.1016/S0370-1573(00)00110-1
35. K. Subramanian, Astron. Nachr. **331**, 110 (2010). https://doi.org/10.1002/asna.200911312
36. A.K. Pandey, P.K. Natwariya, J.R. Bhatt, Phys. Rev. D **101**, 023531 (2020). https://doi.org/10.1103/PhysRevD.101.023531
37. J.R. Bhatt, P.K. Natwariya, A.C. Nayak, A.K. Pandey, Eur. Phys. J. C **80**, 334 (2020). https://doi.org/10.1140/epjc/s10052-020-7886-x. arXiv:1905.13486 [astro-ph.CO]
38. A. Bera, K.K. Datta, S. Samui, Mon. Not. R. Astron. Soc. **498**, 918 (2020). https://doi.org/10.1093/mnras/staa1529. https://www.academic.oup.com/mnras/article-pdf/498/1/918/33718630/staa1529.pdf
39. P.J.E. Peebles, Astrophys. J. **153**, 1 (1968). https://doi.org/10.1086/149628
40. F.H. Shu, The physics of astrophysics. Volume II: Gas dynamics. (ISBN 0-935702-65-2, 1992) http://adsabs.harvard.edu/abs/1992pavi.book.....S
41. D.R.G. Schleicher, R. Banerjee, R.S. Klessen, Phys. Rev. D **78**, 083005 (2008). https://doi.org/10.1103/PhysRevD.78.083005
42. K. Lawson, A. Zhitnitsky, Phys. Dark Universe **24**, 100295 (2019). https://doi.org/10.1016/j.dark.2019.100295
43. K. Lawson, A.R. Zhitnitsky, Phys. Lett. B **724**, 17 (2013). https://doi.org/10.1016/j.physletb.2013.05.070
44. D.G. Levkov, A.G. Panin, I.I. Tkachev, Phys. Rev. D **102**, 023501 (2020). https://doi.org/10.1103/PhysRevD.102.023501
45. R.H. Mebane, J. Mirocha, S.R. Furlanetto, Mon. Not. R. Astron. Soc. **493**, 1217 (2020). https://doi.org/10.1093/mnras/staa280
46. T. Moroi, K. Nakayama, Y. Tang, PLB **783**, 301 (2018). https://doi.org/10.1016/J.PHYSLETB.2018.07.002
47. D. Aristizabal Sierra, C.S. Fong, PLB **784**, 130 (2018). https://doi.org/10.1016/J.PHYSLETB.2018.07.047
48. R. Brandenberger, B. Cyr, R. Shi, J. Cosmol. Astropart. Phys. **2019**, 009 (2019). https://doi.org/10.1088/1475-7516/2019/09/009
49. M. Chianese, P. Di Bari, K. Farrag, R. Samanta, Phys. Lett. B **790**, 64 (2019). https://doi.org/10.1016/j.physletb.2018.09.040
50. T. Venumadhav, L. Dai, A. Kaurov, M. Zaldarriaga, PRD **98**, 103513 (2018). https://doi.org/10.1103/PhysRevD.98.103513
51. G.B. Field, Proc. IRE **46**, 240 (1958). https://doi.org/10.1109/JRPROC.1958.286741
52. S.R. Furlanetto, J.R. Pritchard, MNRAS **372**, 1093 (2006). https://doi.org/10.1111/j.1365-2966.2006.10899.x
53. A. Fialkov, R. Barkana, Mon. Not. R. Astron. Soc. **486**, 1763 (2019). https://doi.org/10.1093/mnras/stz873
54. I. Reis, A. Fialkov, R. Barkana, Mon. Not. R. Astron. Soc. (2020). https://doi.org/10.1093/mnras/staa3091
55. Y. Yang, Phys. Rev. D **98**, 103503 (2018). https://doi.org/10.1103/PhysRevD.98.103503
56. A. Banet, R. Barkana, A. Fialkov, O. Guttman, Quantiles as robust probes of non-gaussianity in 21-cm images. Mon. Not. R. Astron. Soc. Lett., **503**(1), 1221–1232 (2021). https://doi.org/10.1093/mnras/stab318
57. S.A. Wouthuysen, apj **57**, 31 (1952). https://doi.org/10.1086/106661

58. C.M. Hirata, MNRAS **367**, 259 (2006). https://doi.org/10.1111/j.1365-2966.2005.09949.x
59. A. Mesinger, S. Furlanetto, R. Cen, MNRAS **411**, 955 (2011). https://doi.org/10.1111/j.1365-2966.2010.17731.x
60. M. Zaldarriaga, S.R. Furlanetto, L. Hernquist, Astrophys. J. **608**, 622 (2004). https://doi.org/10.1086/386327
61. Planck Collaboration et al., Planck 2018 results. vi. cosmological parameters. (2018). arXiv:1807.06209 [astro-ph.CO]. https://www.ui.adsabs.harvard.edu/abs/2018arXiv180706209P
62. R. Barkana, N.J. Outmezguine, D. Redigolo, T. Volansky, PRD **98**, 103005 (2018). https://doi.org/10.1103/PhysRevD.98.103005
63. G.B. Field, apj **129**, 536 (1959). https://doi.org/10.1086/146653
64. A. Kogut, D.J. Fixsen, S.M. Levin, M. Limon, P.M. Lubin, P. Mirel, M. Seiffert, J. Singal, T. Villela, E. Wollack, C.A. Wuensche, Astrophys. J. **734**, 4 (2011). https://doi.org/10.1088/0004-637x/734/1/4
65. S.K. Sethi, B.B. Nath, K. Subramanian, MNRAS **387**, 1589 (2008). https://doi.org/10.1111/j.1365-2966.2008.13302.x
66. Y. Ali-Haimoud, C.M. Hirata, Phys. Rev. D **83**, 043513 (2011). https://doi.org/10.1103/PhysRevD.83.043513
67. K. Jedamzik, Vcv Katalinić, A.V. Olinto, Phys. Rev. D **57**, 3264 (1998). https://doi.org/10.1103/PhysRevD.57.3264
68. K.E. Kunze, E. Komatsu, JCAP **2014**, 009 (2014). https://doi.org/10.1088/1475-7516/2014/01/009
69. K. Subramanian, J.D. Barrow, Phys. Rev. D **58**, 083502 (1998). https://doi.org/10.1103/PhysRevD.58.083502. arXiv:astro-ph/9712083
70. A. Mack, T. Kahniashvili, A. Kosowsky, Phys. Rev. D **65**, 123004 (2002). https://doi.org/10.1103/PhysRevD.65.123004
71. C. Caprini, R. Durrer, T. Kahniashvili, Phys. Rev. D **69**, 063006 (2004). https://doi.org/10.1103/PhysRevD.69.063006
72. R. Ghara, G. Mellema, MNRAS **492**, 634 (2019). https://doi.org/10.1093/mnras/stz3513
73. J. Mirocha, S.R. Furlanetto, MNRAS **483**, 1980 (2019). https://doi.org/10.1093/mnras/sty3260
74. A. Mesinger, A. Ferrara, D.S. Spiegel, MNRAS **431**, 621 (2013). https://doi.org/10.1093/mnras/stt198
75. A. Fialkov, A. Cohen, R. Barkana, J. Silk, MNRAS **464**, 3498 (2016). https://doi.org/10.1093/mnras/stw2540
76. J. Park, A. Mesinger, B. Greig, N. Gillet, MNRAS **484**, 933 (2019). https://doi.org/10.1093/mnras/stz032
77. E.D. Kovetz, V. Poulin, V. Gluscevic, K.K. Boddy, R. Barkana, M. Kamionkowski, PRD **98**, 103529 (2018). https://doi.org/10.1103/PhysRevD.98.103529
78. J. Mirocha, G.J.A. Harker, J.O. Burns, Astrophys. J. **813**, 11 (2015). https://doi.org/10.1088/0004-637x/813/1/11
79. G.J.A. Harker, J. Mirocha, J.O. Burns, J.R. Pritchard, Mon. Not. R. Astron. Soc. **455**, 3829 (2015). https://doi.org/10.1093/mnras/stv2630
80. X. Asselin, G. Girardi, P. Salati, A. Blanchard, Nucl. Phys. B **310**, 669 (1988). https://doi.org/10.1016/0550-3213(88)90098-3
81. M. Shiraishi, H. Tashiro, K. Ichiki, Phys. Rev. D **89**, 103522 (2014). https://doi.org/10.1103/PhysRevD.89.103522
82. Planck Collaboration et al., A&A **571**, A16 (2014). https://doi.org/10.1051/0004-6361/201321591